LASER INTERFEROMETER GRAVITATIONAL WAVE OBSERVATORY
- LIGO -
CALIFORNIA INSTITUTE OF TECHNOLOGY
MASSACHUSETTS INSTITUTE OF TECHNOLOGY

Technical Note	**LIGO-T2300146–v1**	2023/09/18

Developing spatially-tunable adaptive optics for LIGO

Celeste Virador

California Institute of Technology
LIGO Project, MS 18-34
Pasadena, CA 91125
Phone (626) 395-2129
Fax (626) 304-9834
E-mail: info@ligo.caltech.edu

Massachusetts Institute of Technology
LIGO Project, Room NW22-295
Cambridge, MA 02139
Phone (617) 253-4824
Fax (617) 253-7014
E-mail: info@ligo.mit.edu

LIGO Hanford Observatory
Route 10, Mile Marker 2
Richland, WA 99352
Phone (509) 372-8106
Fax (509) 372-8137
E-mail: info@ligo.caltech.edu

LIGO Livingston Observatory
19100 LIGO Lane
Livingston, LA 70754
Phone (225) 686-3100
Fax (225) 686-7189
E-mail: info@ligo.caltech.edu

http://www.ligo.caltech.edu/

1 Introduction

Gravitational waves (GW) were first predicted by Albert Einstein in his General Theory of Relativity. Their first direct detection was in 2015 by the Laser Interferometer Gravitational-wave Observatory (LIGO), through the response of free test masses (mirrors) to the strain of spacetime. The distance between these test masses can be measured by a laser and calculated from the phase difference of the returning beam. The Advanced LIGO detectors are dual-recycled Fabry-Perot Michelson interferometers. [2] The Fabry-Perot cavities reflect the laser back and forth through the arms of the detector, extending the arms to increase the laser's interaction with the gravitational wave and amplifying the existing GW signal. This amplification is also done through signal recycling.

Sources of gravitational waves include pulsars, transients such as the mergers/inspirals of black holes and neutron stars, and binary systems. Higher sensitivity GW measurements provide more information on the origins and development of these sources, and may contribute discoveries of new astrophysical phenomena. The observation of gravitational radiation from non-discrete sources such as the cosmic expansion of the early universe and the Big Bang is a goal that requires the development of higher sensitivity detectors.

Increasing stored power in the LIGO interferometers decreases quantum shot noise at high frequencies [2]; however, this gives rise to undesirable thermally-induced distortions due absorption of power. Absorption in the coatings of the test masses results in a radial temperature gradient [2] and causes unwanted lensing effects and surface deformations. These cause wavefront distortions, which in turn reduce the amplification of the gravitational wave signal and increase noise at the readout photodiode. Such distortions are currently compensated by the Thermal Compensation System (TCS). The TCS measures the magnitude and spatial distribution of any wavefront distortions, and compensates for induced sagitta changes and wavefront distortions within the test masses.

Uniform absorption refers to the absorption of the main laser beam caused by a spatially invariant absorption coefficient across the high-reflectivity surface of the optic. [3] TCS is designed to compensate for uniform absorption. Non-uniform absorption involves higher spatial-frequency absorption caused by features such as point absorbers, or non-uniform coating absorption and emissivity. Such non-uniform absorption induces distortions causing power to scatter from the fundamental mode into higher order spatial modes [3], which can be enhanced or suppressed by arm cavity gain.

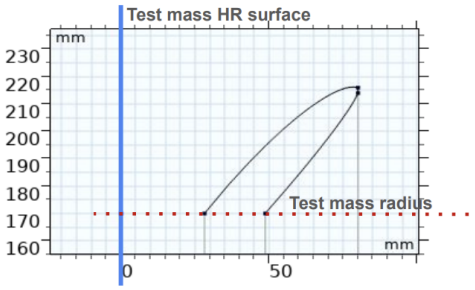

Figure 1: FroSTI Reflector System Design [5]

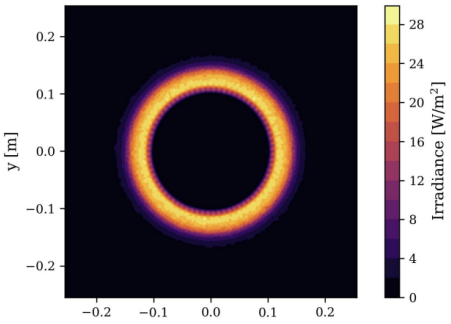

Figure 2: FroSTI Radiance Profile [5]

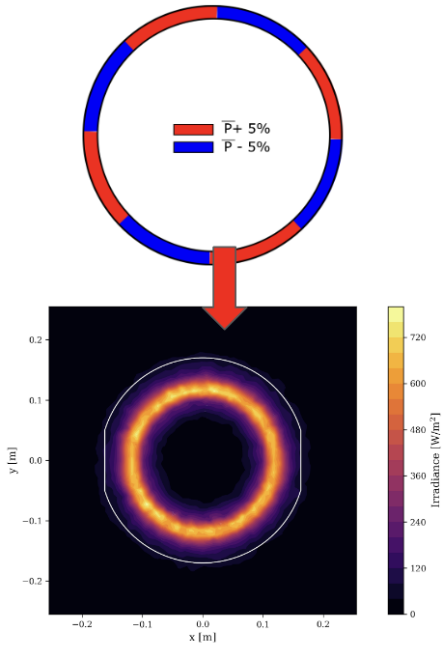

Figure 3: FroSTI Radiance Profile with Variance in Individual Heating Units [4]

The front-surface-type irradiator (FROSTI) is a prototype actuator designed for aLIGO which consists of a ring heater mounted in front of the test masses. The ring heater is comprised of eight sub-units, each consisting of a heater segment and elliptical reflectors. FROSTI uses the asymmetric elliptical profile to deliver IR radiation effectively to the mirror surface, using nonimaging optics design principles (see Figure 1).

FROSTI's initial design targets the enhanced loss of the fundamental mode to the 7th order mode by point-absorbers [4] and will also compensate for the non-spherical surface deformation due to coating absorption. FROSTI demonstrated its ability to constrain radiation radially (see Figure 2). It however does not constrain rays azimuthally, as shown in Figure 3. Simulations of the FROSTI system show that varying radiation across the individual heater units does not produce an exact correspondence of heating in target regions on the test mass.

2 Section 2: Objective

The objective of this project was to address non-uniform absorption-induced distortion by designing new FROSTIs to generate more complex and precise heating profiles. This project aimed to modify the current FROSTI design to improve localization of radiation within the target regions associated with individual heating units, improving azimuthal confinement while also maintaining radial confinement. The specific design modifications focused on the design and optimization of reflective edge surfaces to be implemented within the individual heater units.

An efficient and realistic heater arrangement was a simultaneous goal throughout the design process.

3 Section 3: Set Up For Design Modifications

The simulations of the FROSTI ring heater and ring heater elements were performed in COMSOL Multiphysics, using the Ray Tracing and Optimization Modules.

Before beginning the design process, the current spread of radiation/level of radiation confinement from an individual heater unit ($\frac{1}{8}$ of the full heater ring) needed to be confirmed. The $\frac{1}{8}$ heater unit was simulated within COMSOL, with an eighth of the associated power from the full ring heater and an eighth of the associated rays from the full heater model. This was to decrease the time associated with the simulation for ease of analysis. A 2D Surface Plot of the irradiance was produced from the ray tracing simulation, shown in Figure 4.

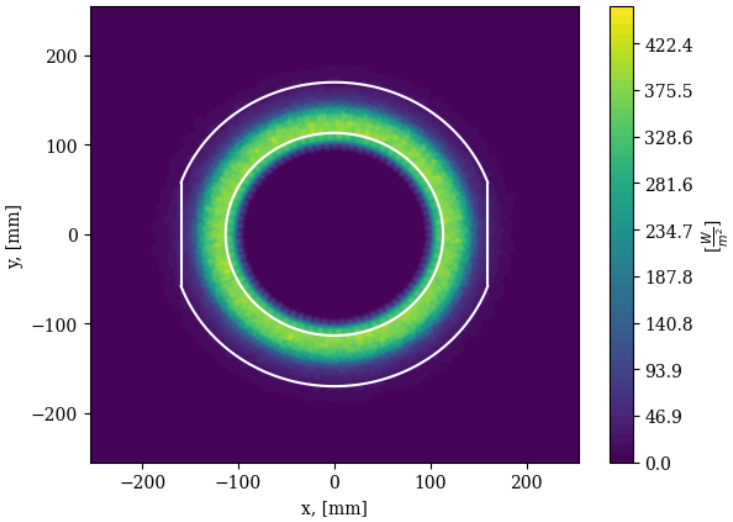

Figure 4: Irradiance Surface Plot from Full Heater Unit

Two distributions were chosen to characterize the 2D Surface Irradiance plot shown in Figure 4: the angular distribution of average irradiance and the radial distribution of average irradiance. These were created by compressing one dimension into an average; for example, in the case of the angular distribution, the irradiance was averaged in the radial dimension (Figure 5).

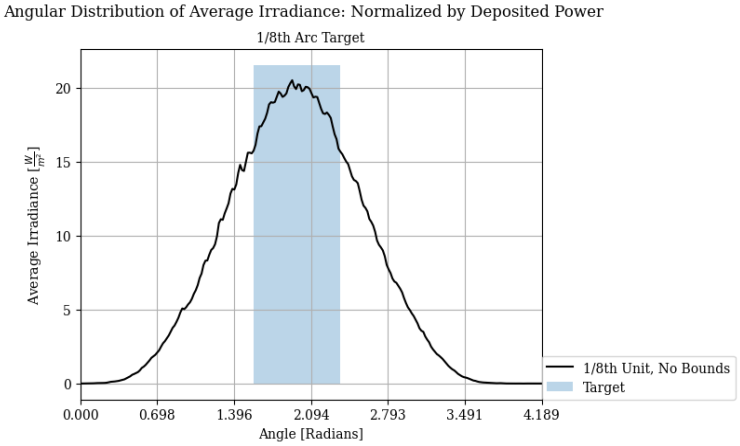

(a)

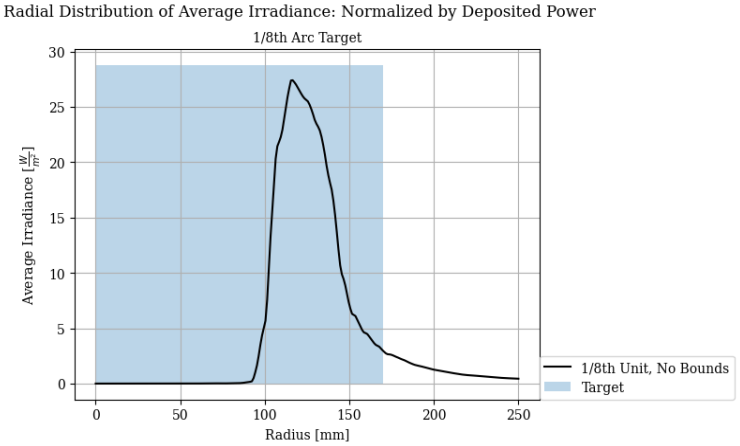

(b)

Figure 5: (a) Angular and (b) Radial Distributions of Average Irradiance for $\frac{1}{8}$ Arc Heater Unit

After establishing these two spread characterizations, the heater units were further simplified from arc models to linear models, the length of which was identified from the arc length of the original model. The heater strip's radius to the center of the rotation for the original full ring heater unit was used to characterize this arc length ($r_{Full\ Heater} = 216\,mm$) (Figure 6).

This modification to the heater unit models also modified the characterization of radiation spread; the angular and radial spreads of average irradiance were then converted to horizontal and vertical distributions of average irradiance (Figure 7).

The final step taken before edge surface design modifications began was the division of the $\frac{1}{8}$ heater unit into four sub-units. This was motivated originally by an examination of the extreme rays produced by the heater unit, as pictured below in Figure 8. These would be the most extreme rays to possibly still interact with any edge coverings designed.

Comparing between the $\frac{1}{8}$ heater unit and a quarter of the $\frac{1}{8}$ unit, or a $\frac{1}{32}$ heater unit, the $\frac{1}{8}$ heater unit produces this extreme ray at a larger angle (due to its longer length). This difference in angle between the two units suggested that it may be easier to design edge

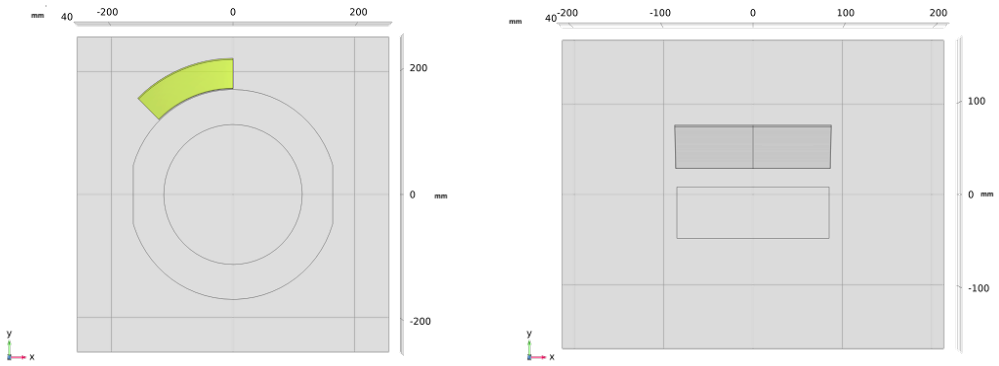

(a) (b)

Figure 6: Overhead views of (a) $\frac{1}{8}$ Arc Heater Unit and (b) $\frac{1}{8}$ Linear Heater Unit

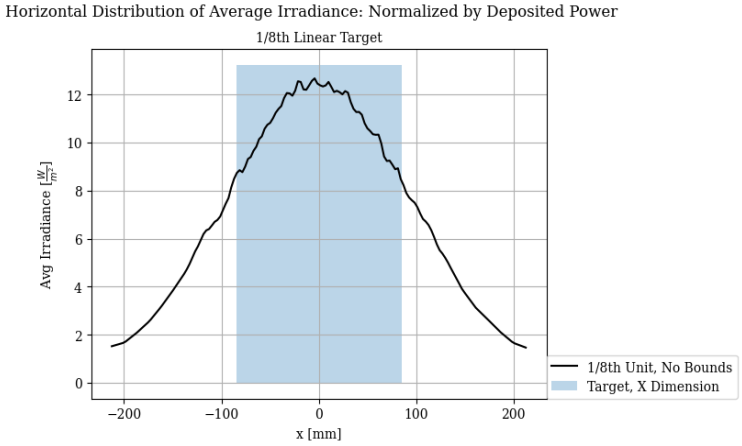

(a)

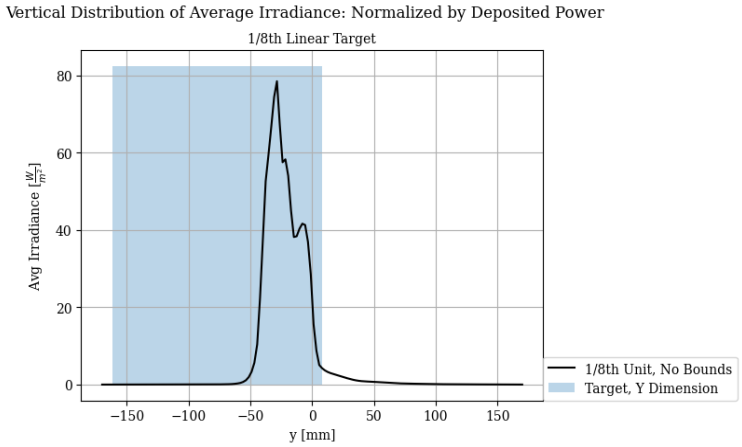

(b)

Figure 7: (a) Horizontal distribution and (b) Vertical distribution of average irradiance produced from linear $\frac{1}{8}$ heater unit

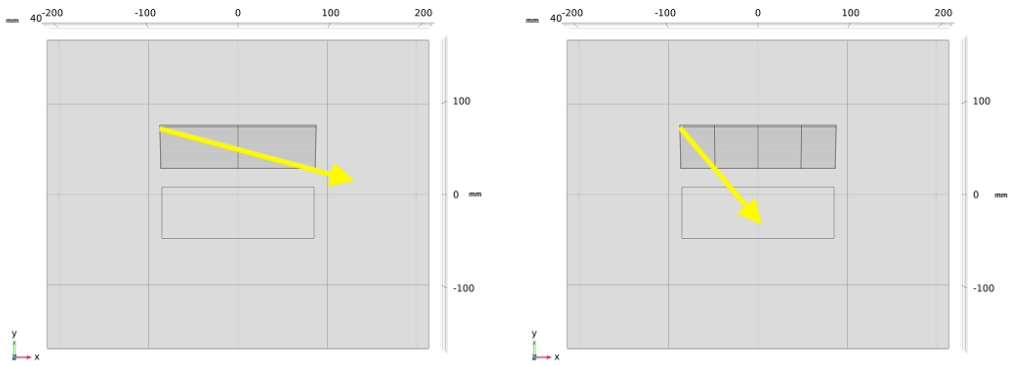

(a) (b)

Figure 8: Extreme rays emitted by (a) linear $\frac{1}{8}$ heater unit and (b) 4 $\frac{1}{32}$ heater units

surfaces that would redirect the extreme rays from the $\frac{1}{32}$ heater unit back to its associated target region. The decision was then made to focus on designing reflective edge surfaces for the the $\frac{1}{32}$ heater unit (linear model), with a goal of improving the confinement of the produced irradiance within a target of the same width as the $\frac{1}{32}$ heater unit.

$$Width,\ Target = 2 * pi * (r_{heater}) * 1/32$$

The height (in the y-dimension) of the target was the radius of the original arc target (170 mm).

4 Section 4: Edge Surface Design

4.1 Flat Edges

The first type of edge surfaces tested on the $\frac{1}{32}$ heater unit were flat, reflective edges.

Flat reflective surfaces produced the surface irradiance plot in Figure 9b and the average irradiance distributions in Figure 10.

Visually, the tails of the horizontal distribution of average irradiance for the flat reflective edge model are flattened in comparison to the model without bounds (to be referred to in the future as the No Bounds Model). The width of the distribution also appears to be smaller. The tails of the vertical distribution of average irradiance also appear to be flattened compared to the No Bounds model.

To confirm this, the horizontal and vertical distributions were compressed into two figures of merit respectively. For the horizontal distribution, the Full Width, Half Max (FWHM) value was used to characterize the width of the distribution, and the area under the tails (or the area under the portion of the curve outside of the target bounds) characterized the behavior of the tails. For the vertical distribution, the standard deviation of the distribution and the area under the tails characterized the curves. The values of these figures of merit are included in the tables below.

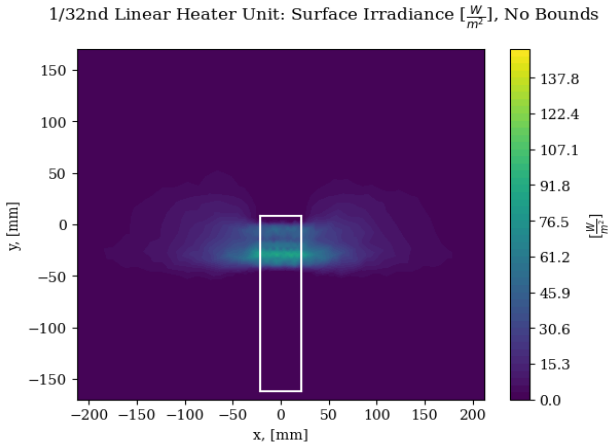

(a)

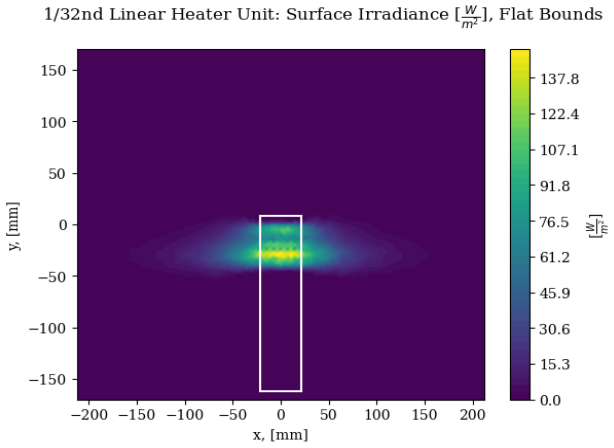

(b)

Figure 9: Surface Irradiance Plots from a) an unbounded, linear $\frac{1}{32}$ unit and b) a flat bounded, linear $\frac{1}{32}$ unit

Model	FWHM (Horizontal Spread)	Tail Area (Horizontal Spread)
No Bounds	168.699	2324.171
Flat Bounds	86.709	1827.449

Model	Standard Deviation (Vertical Spread)	Tail Area (Vertical Spread)
No Bounds	27.737	390.7
Flat Bounds	12.407	3.758

Using these values, the improvement in radiation confinement produced by the model with flat, reflective bounds is confirmed.

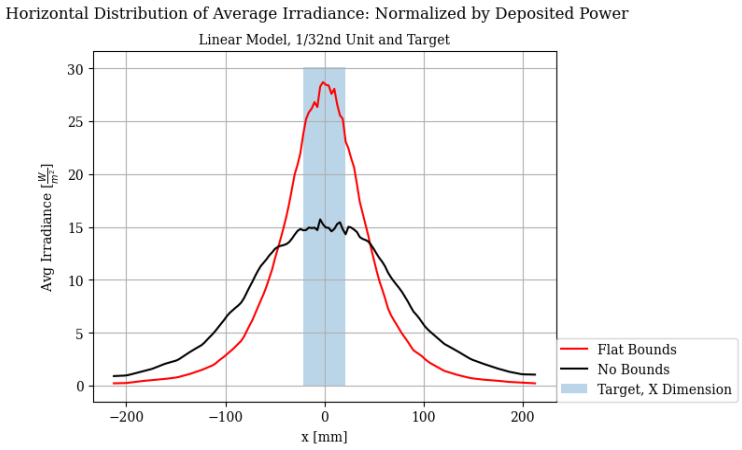

(a)

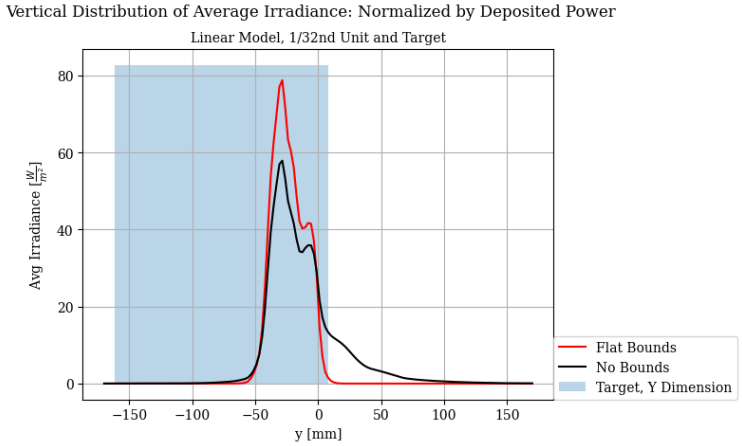

(b)

Figure 10: (a) Horizontal and (b) Vertical Distributions of Average Irradiance from Unbounded and Flat Bounded Models

4.2 Parabolic Edges

After confirming that it was possible to improve upon the confinement of radiation produced by a unbounded heater unit with the introduction of flat reflective bounds, the next step in the design process involved the design of parabolic bounds.

The parabolic edge surfaces were designed with the goal of maintaining the length of the heater unit's source. The method of design is as follows:

1. A parabola is defined parametrically as:

$$x = p1 \cdot s, y = p2 \cdot s^2$$

2. The parabola is then moved such that its vertex rests on the heater unit's source (heater strip) at the x-locations of $\pm pi * (r_{heater}) * 1/32$.

3. The parabola is moved upwards by, at minimum, 1 mm. This is to enable the Partitioning of the heater unit by the parabola through COMSOL.

4. The parabola is then linearly extruded through the heater unit and used to partition it.

The resulting heater unit is shown in Figure 11.

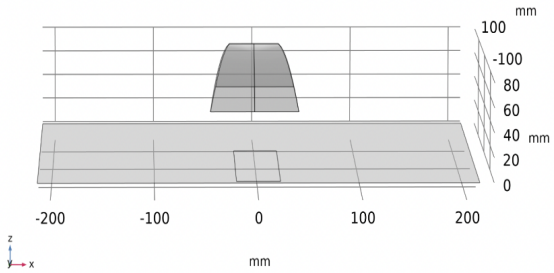

Figure 11: $\frac{1}{32}$ heater unit, with parabolic edge bounds

In the parabolic edge surfaces, there are generally two parameters and thus two degrees of freedom, p1 and p2.

Three different models were created using this method of design. The first involved the extrusion of the parabolic surface through the heater, at the location of where the $\frac{1}{32}$ heater unit's heater source would end (Model 1), as seen in Figure 12.

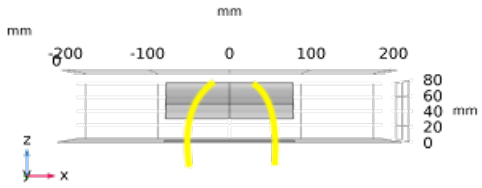

Figure 12: Model 1

The second model, Model 2, allowed the parabola generating the surface to rotate within the z-x plane, as seen in Figure 13; a new variable to describe this rotation, phi_{parab}, was developed.

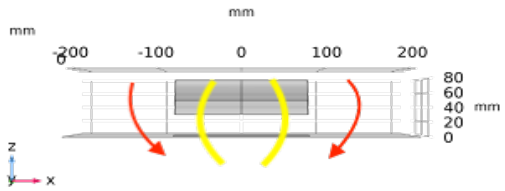

Figure 13: Model 2

The third and final model involved the set rotation of the original parabola's plane along the axis of the heater, as shown in Figure 14 (Model 3). The parabola was then extruded

through the heater; the parabola had to have a slightly larger displacement from the heater source compared to Models 1/2 in order to be able to partition the heater unit.

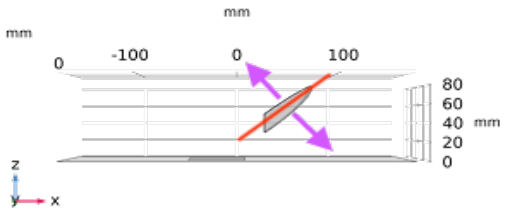

Figure 14: Model 3

4.3 Optimization

The degrees of freedom were then explored via optimization. COMSOL's Optimization Module was used, using Nelder-Mead as the method.

Before the optimization module was used, an objective function was defined and parameter sweeps were conducted to inform the general starting values and constrain the parameters for the optimization.

Within the simulation, the target plane onto which radiation was deposited was divided into two sections: an Inner Target and an Outer Target. The ratio of the power deposited on the Outer Target and the Inner Target was chosen as the objective function to minimize.

$$Objective\ Function = Power_{Deposited\ on\ Outer\ Target} / Power_{Deposited\ on\ Inner\ Target}$$

Parameter sweeps were first run for Model 1; the figures of merit for characterizing radiation confinement were chosen to be the tail areas of the distribution curves outside of the vertical and horizontal targets.

An optimization study for Model 1 was then conducted, leading to optimized values for p1 and p2:

Model	p1	p2
Model 1	43.326	5.5828

Instead of running a general parameter sweep for Model 2, an optimization study was conducted, with the optimized values from Model 1 serving as the initial values of p1 and p2. A third variable, phi_{parab}, was then allowed to vary. The optimized values for p1, p2, and phi_{parab} are recorded in Row 2 of the following table:

Model	p1	p2	phi_{parab}
Model 1	43.326	5.5828	Not Applicable
Model 2	44.5259	8.69	0.313588

Finally, a parameter sweep was run on Model 3, and then an optimization was conducted, leading to leading to optimized values for p1 and p2 as follows in Row 3 in the table below:

Model	p1	p2	phi_{parab}
Model 1	43.326	5.5828	Not Applicable
Model 2	44.5259	8.69	0.313588
Model 3	90.607	12.58	Not Applicable

5 Section 5: Results

The horizontal and angular distributions of average irradiation show visible differences in the performances of each model; however, comparison of the vertical and radial spreads is difficult to interpret visibly. Figures of merit characterizing the four distributions used in this project were determined as follows.

For the horizontal and angular spreads of irradiation, the Full Width, Half Max value (FWHM) and area under the tails were used to characterize the width of the distributions and their tail behaviors. For the vertical and radial spreads, the standard deviation and area under the tails were used.

5.1 $\frac{1}{32}$ Linear Model and Target

All three parabolic edge models produce a visible flattening in the tails of the horizontal spread of average irradiance compared to both the flat bounded model and the model without bounds (Figure 15). A more thorough comparison of each model's confinement of radiation is present in the figures of merit plots in Figure 16, and in the following tables.

Model	FWHM (Horizontal Spread)	Tail Area (Horizontal Spread)
No Bounds	168.699	2324.171
Flat Bounds	86.709	1827.449
Model 1	80.843	1646.232
Model 2	77.315	1609.149
Model 3	82.968	1618.889

Model	Standard Deviation (Vertical Spread)	Tail Area (Vertical Spread)
No Bounds	27.737	390.7
Flat Bounds	12.407	3.758
Model 1	13.5	1.937
Model 2	14.959	2.106
Model 3	11.482	0.246

Model 2 and Model 3 perform best in horizontal and vertical confinement, respectively.

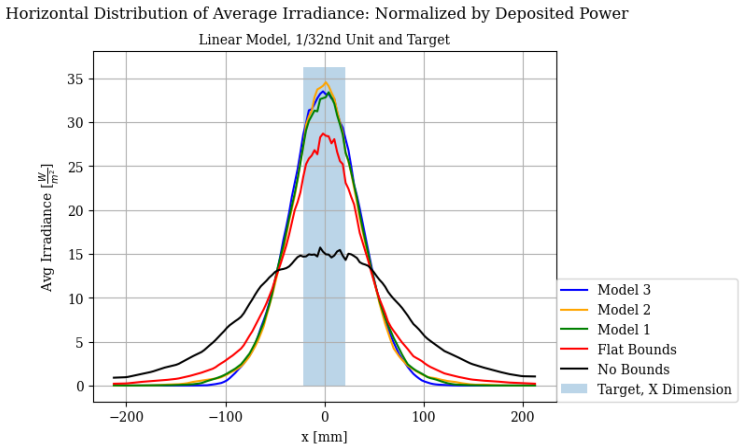

(a)

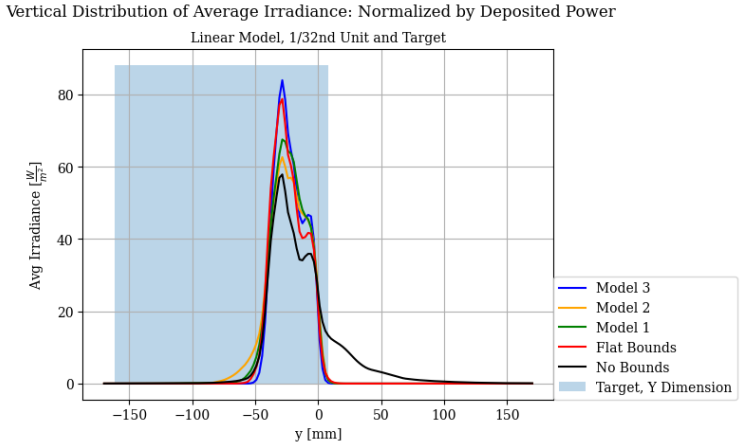

(b)

Figure 15: (a) Horizontal and (b) Vertical Distributions of Average Irradiance, $\frac{1}{32}$ Linear Heater Unit

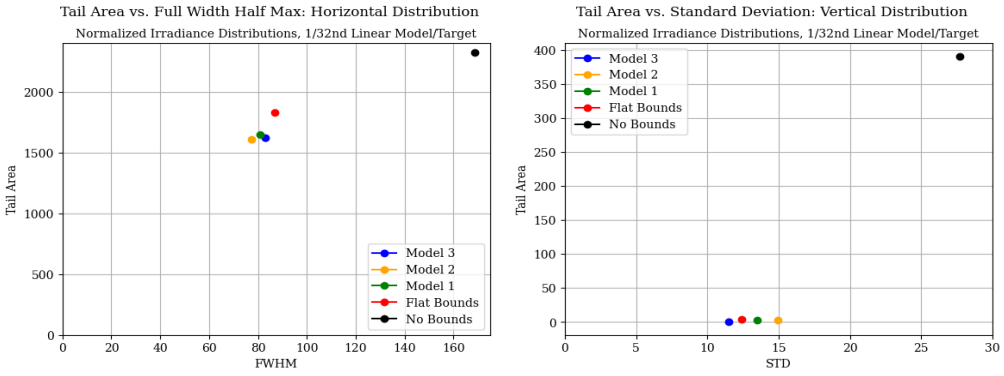

(a) (b)

Figure 16: Figures of Merit for (a) Horizontal and (b) Vertical Distributions of Average Irradiance, $\frac{1}{32}$ Heater Unit

Another, more qualitative confirmation of the effect produced by the different edge models is the horizontal and vertical spread of edge rays - these are the rays that interact with the edge reflectors at some point in their trajectory. These rays were identified by simulating the spread of rays from models with absorptive edge bounds, and then subtracting the associated surface irradiance plot from a surface irradiance plot produced by a fully reflective model (Figure 17).

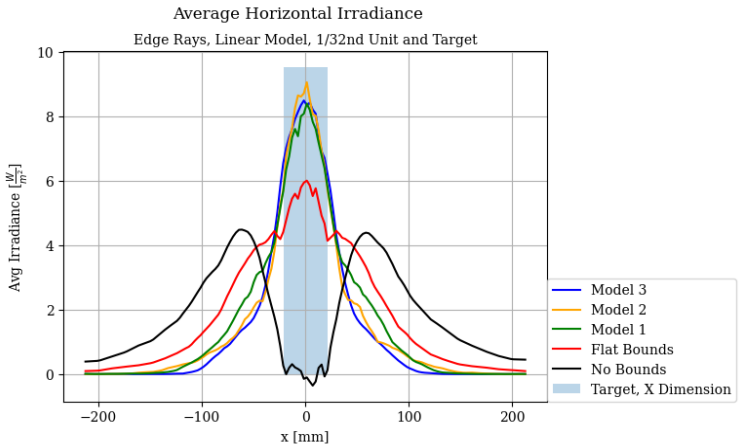

(a)

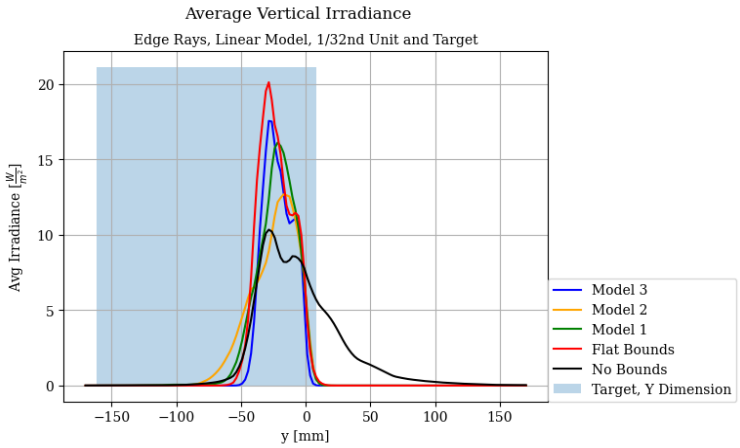

(b)

Figure 17: a) Horizontal and b) Vertical Distributions of Average Irradiance, from Edge Rays produced by a linear $\frac{1}{32}$ heater unit

Visible in Figure 17a is the gradual collection of edge rays towards/into the target region. The tails of the horizontal distributions produced by the three parabolic models are lower than those produced by the flat bounds and the model without bounds. The three parabolic bounds also produce higher peaks of the distribution within the horizontal target bounds, showing the redirection of the edge rays into the target region. For the vertical distribution, most obviously for Model 3, the tails are flattened with the parabolic models compared to the flat and no bounded models.

5.2 $\frac{1}{32}$ Arc Model and Target

The three parabolic models were then simulated on arc $\frac{1}{32}$ heater units, producing the angular and radial distributions of average irradiance seen in Figure 18.

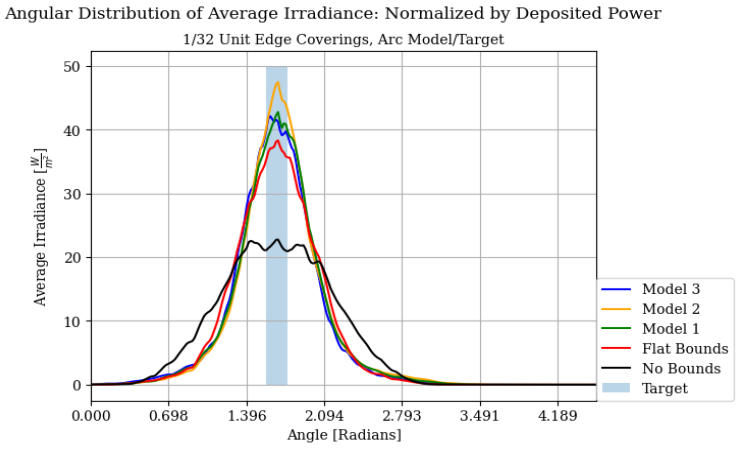

(a)

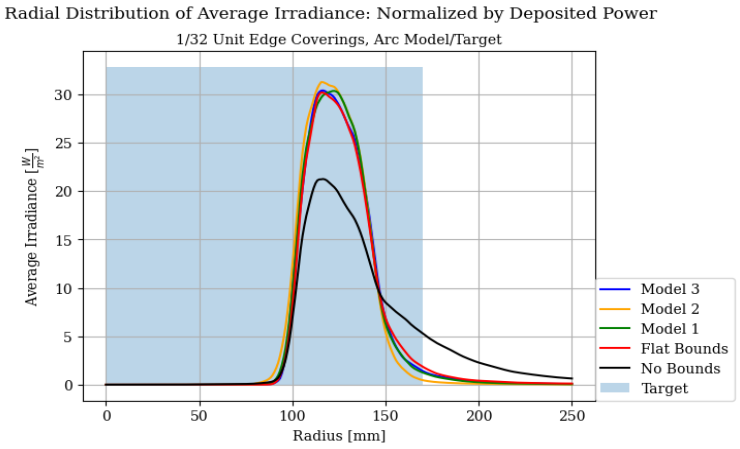

(b)

Figure 18: (a) Angular and (b) Radial Distributions of Average Irradiance, $\frac{1}{32}$ Arc Heater Unit

Model	FWHM (Angular Spread)	Tail Area (Angular Spread)
No Bounds	1.227	24.606
Flat Bounds	0.775	24.175
Model 1	0.646	23.82
Model 2	0.562	23.667
Model 3	0.667	23.666

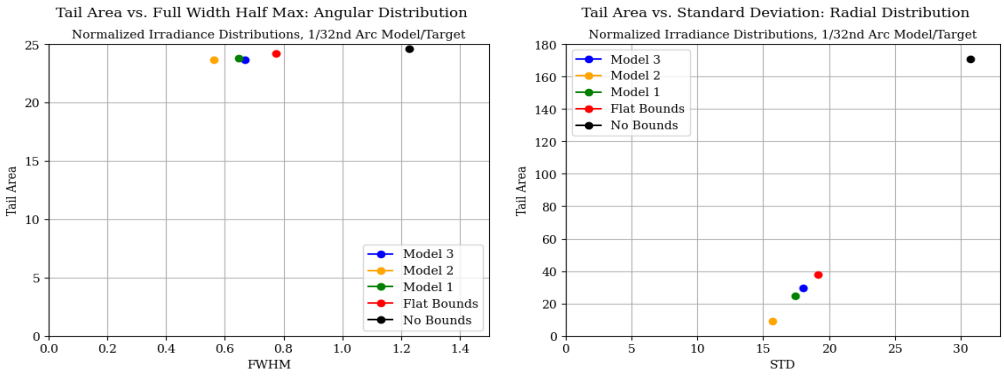

(a) (b)

Figure 19: Figures of Merit for (a) Angular and (b) Radial Distributions of Average Irradiance, $\frac{1}{32}$ Arc Heater Unit

Model	Standard Deviation (Radial Spread)	Tail Area (Radial Spread)
No Bounds	30.74	171.023
Flat Bounds	19.162	38.004
Model 1	17.441	24.499
Model 2	15.724	9.358
Model 3	18.066	29.811

The model that performed the best in both horizontal and vertical confinement, as shown by the horizontal and vertical distribution figure of merit plots (Figure 19), is Model 2.

5.3 $\frac{1}{8}$ Linear Target

Returning to the scale of the original heater units, four $\frac{1}{32}$ heater units, each with a quarter of the total power of a $\frac{1}{8}$ heater unit, were arranged linearly. The linear $\frac{1}{32}$ target was changed to a $\frac{1}{8}$ target. The horizontal and vertical distributions of irradiance produced from this arrangement of heaters with parabolic bounds is shown in Figure 20, as well as those produced by four flat bounded $\frac{1}{32}$ heater units and an unbounded $\frac{1}{8}$ heater unit.

Visibly, the tails of the horizontal distribution produced by Model 3 are the flattest; the widths are not as clearly identified. The vertical distributions cannot be easily distinguished from one another.

The figures of merit (Figure 21) for the horizontal spread of average irradiance show the lowest tail area value for Model 3; Model 2 and Model 3 have smaller FWHM values, but larger tail values. For the vertical spread of average irradiance, the model with flat reflective bounds performs well in vertical confinement with the smallest standard deviation.

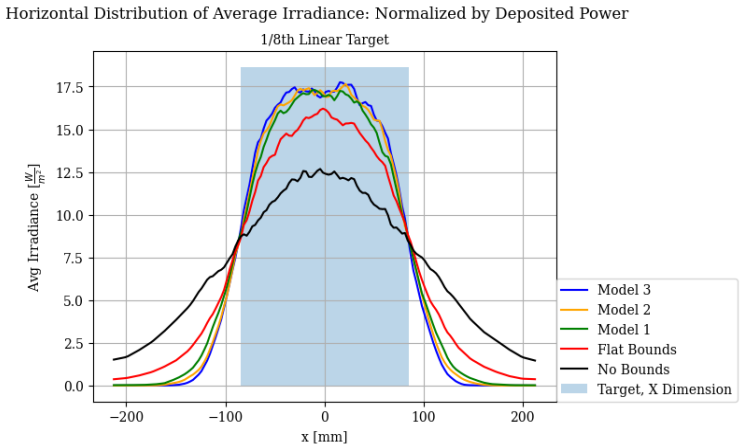

(a)

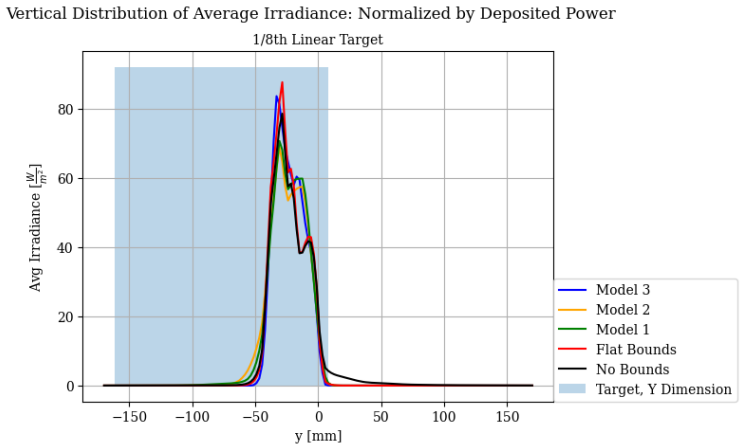

(b)

Figure 20: (a) Horizontal and (b) Vertical Distributions of Average Irradiance, $\frac{1}{8}$ Linear Target

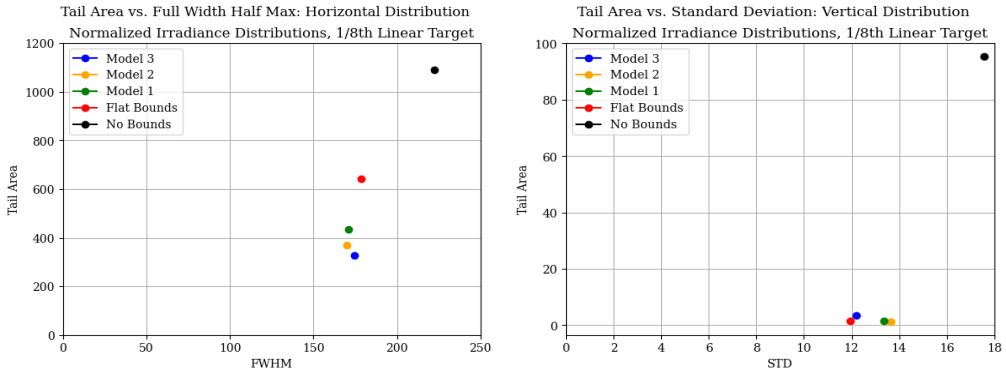

(a) (b)

Figure 21: Figures of Merit for (a) Horizontal and (b) Vertical Distributions of Average Irradiance, $\frac{1}{8}$ Linear Heater Unit

Model	FWHM (Horizontal Spread)	Tail Area (Horizontal Spread)
No Bounds	222.404	1091.599
Flat Bounds	178.706	640.98
Model 1	170.884	433.243
Model 2	170.034	370.728
Model 3	174.625	328.319

Model	Standard Deviation (Vertical Spread)	Tail Area (Vertical Spread)
No Bounds	17.581	95.395
Flat Bounds	11.952	1.621
Model 1	13.376	1.535
Model 2	13.664	1.263
Model 3	12.186	3.417

5.4 $\frac{1}{8}$ Arc Target

Returning to the original target geometry, or a $\frac{1}{8}$ arc target, four arc $\frac{1}{32}$ heater units were assembled to form a full-length $\frac{1}{8}$ arc heater unit. The angular and radial distributions of average irradiance produced by this arrangement of heaters is shown in Figure 22, as well as those from four flat bounded $\frac{1}{32}$ arc heater units and an unbounded $\frac{1}{8}$ arc heater unit.

Visibly, the angular spread of average irradiance produced Model 2 shows the lowest tails out of all of the other models (Figure 22a); Model 2 also produces the lowest tails out of all the radial distributions (Figure 22b).

Model	FWHM (Angular Spread)	Tail Area (Angular Spread)
No Bounds	1.418	15.492
Flat Bounds	0.971	10.755
Model 1	0.876	9.491
Model 2	0.81	7.499
Model 3	0.873	9.442

Model	Standard Deviation (Radial Spread)	Tail Area (Radial Spread)
No Bounds	25.412	96.792
Flat Bounds	19.008	37.453
Model 1	14.242	4.92
Model 2	12.782	0.136
Model 3	15.05	9.114

Based on both angular and radial confinement of radiation, Model 2 performs the best out of all of the parabolic models, and outperforms the flat model (Figure 23).

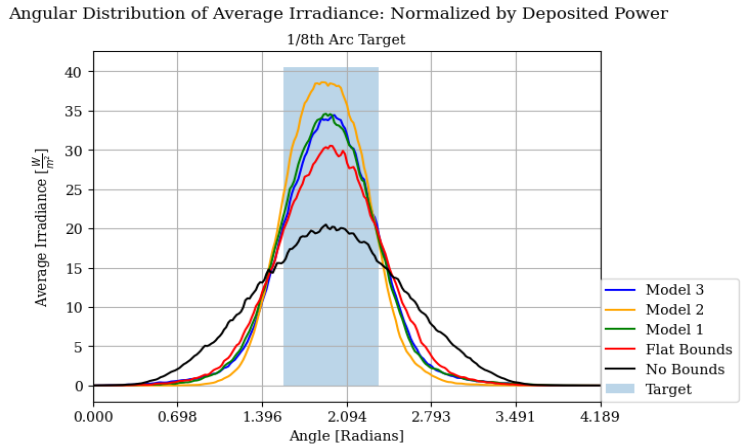

(a)

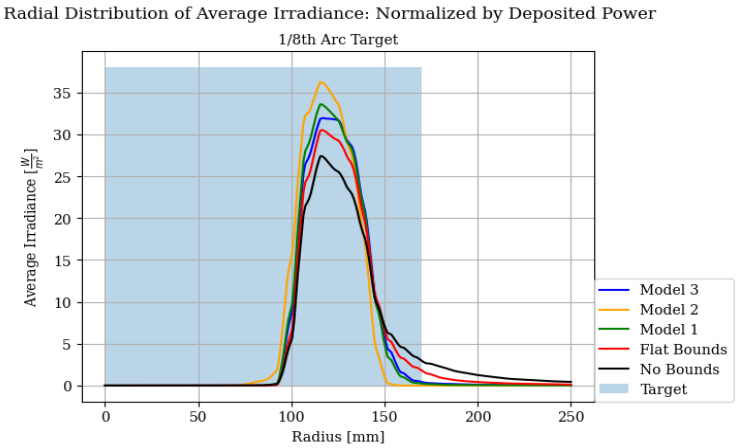

(b)

Figure 22: (a) Angular and (b) Radial Distributions of Average Irradiance, $\frac{1}{8}$ Arc Target

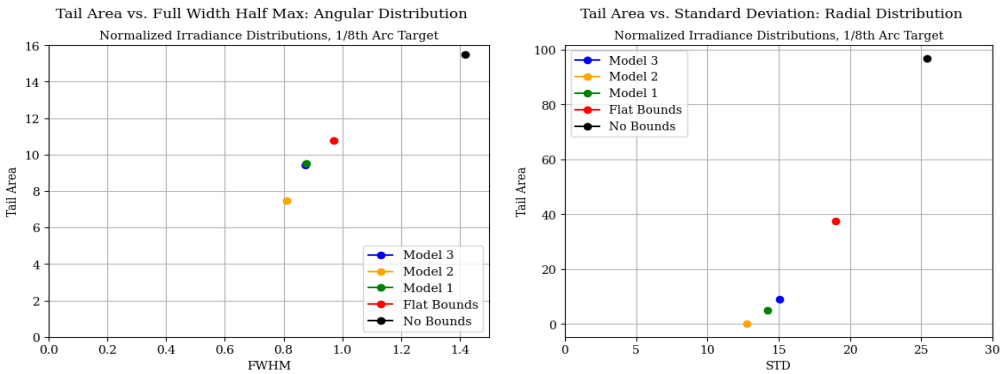

(a) (b)

Figure 23: Figures of Merit for (a) Angular and (b) Radial Distributions of Average Irradiance, $\frac{1}{8}$ Arc Heater Unit

6 Section 6: Future Work and Conclusion

6.1 Future Work, Project Extensions

6.1.1 Edge Design Process Modifications

The current parabolic edge surface design process involved the placement of the parabola on the heater unit's source, to be extruded directly through the heater. However, to effectively partition the heater unit, the parabola needed to be displaced slightly above the source. This allowed the size of the heater unit's source to potentially vary within each of the different models, depending on the curvature of the parabola. In future extensions to this project, a potential goal would be to find a way to more strictly limit/standardize the size of the heater sources.

A related issue was the implementation of parabolic bounds to the $\frac{1}{32}$ units that were arranged linearly/in an arc formation to direct radiation within a $\frac{1}{8}$ target. Because the edge surfaces were not flat, the heaters themselves needed to be shortened in length/arc length to fit four of the $\frac{1}{32}$ units above the target. Exploring a standardized shortened length of the heater units coudl be another future extension to this project.

6.1.2 New Models/Surfaces and Optimization Extensions

Testing the performance of an additional parabolic edge surface model, in which the plane is rotated along the axis and the parabola is free to rotate within the plane, is also a possible project extension. Other surfaces can be explored in a similar vein to the parabolic surfaces; the elliptical concentrator from non-imaging optics could potentially inform elliptical side reflectors. Finally, a more general parametric surface (such as an elliptic paraboloid or an ellipsoid, which have an additional degree of freedom compared to the extruded parabola) could prove a more efficient basis with which to optimize. Issues with this method include, but are not limited to, fitting the edges of this general surface to the cross section of the heater unit. This may be difficult to do analytically.

6.2 Conclusion

The spread of radiation from arc and linear heater units was characterized by horizontal/vertical and angular/radial distributions respectively. The capability of flat, reflective boundaries to localize radiation in the angular dimension and maintain confinement within the radial dimension was identified. An exploration of parabolic surfaces was conducted, and three distinct parabolic edge surface model were designed and optimized. In particular, Model 2 (a parabola free to rotate within the z-x plane) shows promise in the confinement of radiation into a $\frac{1}{8}$ arc target.

References

[1] Rana X Adhikari, et al., *Gravitational Radiation Detection with Laser Interferometry*. arXiv:1305.5188 (2014).

[2] A.F. Brooks, et al., *Overview of Advanced LIGO Adaptive Optics*. arXiv:1608.02934 (2016).

[3] A.F. Brooks, et al., *Point Absorbers in Advanced LIGO*. arXiv:2101.05828 (2021).

[4] Huy Tuong Cao, et al., *Development Status of HOM Ring Heater*. LIGO Presentation, UCR Physics and Astronomy, 2022.

[5] Huy Tuong Cao, et al., *Updates on FroSTI for use in LIGO*. LIGO Presentation, UCR Physics and Astronomy, 2023.

[6] Lun Jiang, Roland Winston, *Asymmetric Design for Compound Elliptical Concentrators (CEC) and its geometric glux implications*. Proc. SPIE 9572, Nonimaging Optics: Efficient Design for Illumination and Solar Concentration XII (2015).

[7] B.S. Sathyaprakash, et al., *Physics, Astrophysics and Cosmology with Gravitational Waves*. Living Reviews in Relativity (2009).

[8] Roland Winston, et al., *Nonimaging optics: a tutorial*. Advances in Optics and Photonics, Vol. 10, Issue 2, pp. 484-511 (2018).